
LIQUID-LIQUID CRITICAL POINT IN PHOSPHORUS

A PREPRINT

Manyi Yang

Istituto Italiano di Tecnologia (IIT)
Via Morego, 30, 16163 Genova GE, Italy

Tarak Karmakar

Istituto Italiano di Tecnologia (IIT)
Via Morego, 30, 16163 Genova GE, Italy

Michele Parrinello*

Istituto Italiano di Tecnologia (IIT)
Via Morego, 30, 16163 Genova GE, Italy

May 3, 2021

ABSTRACT

The study of liquid-liquid phase transition has attracted considerable attention. One interesting example of such phenomenon is phosphorus for which the existence a first-order phase transition between a low density insulating molecular phase and a conducting polymeric phase has been experimentally established. In this paper, we model this transition by an *ab-initio* quality molecular dynamics simulation and explore a large portion of the liquid section of the phase diagram. We draw the liquid-liquid coexistence curve and determine that it terminates into a second-order critical point. Close to the critical point, large coupled structure and electronic structure fluctuations are observed.

*michele.parrinello@iit.it

One phenomenon that has attracted much attention is that of liquid-liquid (LL) phase transitions. Most famously, the existence of such a LL transition terminating in a critical point has been suggested as a possible explanation for the famous water anomalies.¹⁻⁹ Unfortunately the location of this transition in the so called no man’s land has made its experimental study challenging. Besides water, the existence of LL transition has been discussed in a number of other systems.¹⁰⁻¹⁶ However experimental investigations in these systems are also fraught with difficulties since the reported LL transitions occur in a regime of high temperatures and pressures.

Among the many systems for which a LL transition has been reported a most intriguing example is that of liquid phosphorus. Phosphorus is an interesting substance with several practical applications and already in the solid phase, exhibits many allotropes. Thus, it is perhaps not a surprise that also in the liquid state, different structures can be found. Katayama *et al*^{17,18} have reported experimental evidence of the existence of a first-order LL transition as signaled by an abrupt density jump. The low-density phase (LDL) is an insulating fluid whose structural units are P_4 molecules while the high-density phase (HDL) is a conducting fluid whose structure has been described as polymeric. Subsequent experiments have revealed that the slope of the LL transition line in the temperature-pressure (TP) plane is negative.¹⁹ In addition, the existence of a liquid-liquid critical point (LLCP) at $T \geq 2500$ K has been conjectured but so far no firm experimental evidence has been reported.

This obviously calls for simulations that can clarify the behavior of liquid phosphorus and in particular, the existence of a critical point. This task is made difficult by the metal to nonmetal transition that accompanies the LL transition. The change in chemical bonding renders a standard approach to the development of a realistic phosphorus force field challenging. A possible alternative is to use *ab-initio* molecular dynamics simulations in which the forces are computed on-the-fly from accurate electronic structure calculations. Typically the forces are calculated by using density functional theory (DFT) which provides a balance between computational expediency and accuracy. A number of such simulations have been reported, and they all have shown that a DFT-based approach is able to reproduce the existence of the LL transition.^{20,21} A somewhat indirect attempt has also been made at estimating the critical point.^{22,23} Although these simulations are highly illuminating, their computational cost has required some compromise as to the system size, the simulation length, and has allowed only for the limited number of thermodynamic states to be explored.

A way of obtaining *ab-initio* MD accuracy at a limited computational cost was suggested some time ago by Behler and Parrinello.^{24,25} Their idea was to use the generalization capabilities of neural networks (NN) to express the potential energy surface. The parameters of the NN were trained on a relatively large set of DFT calculations performed on

appropriately selected atomic configurations. Since Behler and Parrinello’s work, much progress has been made, and this approach has become very popular.^{26-29,29-32} Here we shall use, as we have done in the recent past,³³⁻³⁵ the Deep MD code.^{36,37} In the case of phosphorus, an approach similar in spirit but based on the Gaussian Kernel representation of the potential has already been used to study its allotropes and liquid state.³⁸ However, the exploration of the high pressure and high temperature part of the phase diagram has been limited.

In the Behler-Parrinello-type of approach, a judicious choice of the training configurations is important. In our case, the choice of configurations is complicated by the fact that a first-order phase transition is a rare event. Therefore, the transition state configurations that are essential for determining the transition barrier between one phase and the other are rarely sampled and are not encoded in the NN. For this reason, when studying rare events, we have proposed to train the NN extracting configurations from an enhanced sampling run where the low probability, but highly important transition state arrangements are sampled.³³⁻³⁵ Furthermore, in the study of phase diagrams, it is convenient to follow Ref.³⁴ and^{39,40} and use a multithermal multibaric (MultiTP) enhanced sampling method. The MultiTP approach allows entire regions of the TP phase diagram to be explored at a computational cost comparable to that of a single standard simulation at a given temperature and pressure. A full description of the technical details can be found in the supporting information (SI). Here we mention only the fact that we use the OPES version of the MultiTP approach.^{41,42} OPES, like many other enhanced sampling methods,⁴³⁻⁴⁵ relies on the definition of a collective variable (CV) whose fluctuations are enhanced by the method.^{42,46} A natural choice would have been to use the density as a CV that is the natural order parameter for the phase transition. However since this CV performed poorly, we choose instead the value of the first peak of the Debye structure factor (see Fig. S2 in SI).⁴⁷ However, most of the time we express our results as a function of the density that is a standard thermodynamic variable.

The strategy for generating the NN training configurations follows the active learning scheme of Ref.^{35,48,49} That is, one first performs a number of standard *ab initio* MD calculations in a grid of thermodynamic conditions. These configurations are used to obtain a first guess of the NN potential. In reality, four slightly different NN models are obtained by starting the NN stochastic optimization of the NN from different initial conditions. One of these models is then used to drive the MultiTP-OPES calculation. Periodically we check whether all four NN models predict similar forces. If the discrepancy between their predictions exceeds a preassigned threshold (see SI), we calculate the DFT energies and forces for those particular configurations and add these data to the training set and at a fixed interval re-train all four NN models. This procedure is continued until no significant discrepancy between the four models is observed. The calculations presented here are based on the SCAN+D3 exchange-correlation model that gives a good

agreement between experiment and theory (see Fig. S6 in SI).

Since our MD calculations are based on a MultiTP approach, we can calculate the system properties in the range of temperatures and pressures that is specified at the beginning of the calculation, without having to perform new simulations. Thus, it is painless to identify the transition line and other significant thermodynamic points. The procedure used to draw the coexistence line is illustrated with the example of the free energy surface behavior as a function of pressure at $T = 2000$ K (see Fig. 1 (left)). At the lower pressure, the LDL phase is more likely while at the high pressure HDL prevails. The location at which they are equally probable defines the pressure where the two liquids coexist at the selected temperature. This behavior is consistent with a first-order transition, and the locus of such coexistence points defines the boundary line between the two phases.

This behavior is to be contrasted with that at $T = 2800$ K, where pressure induces a continuous change from a LDL-like to a HDL-like structure (see Fig. 1 (right)). In this region of the phase diagram one is above the critical point. However, also in this part of the phase diagram a thermodynamically significant line can be drawn. This is the so called Widom line defined as the locus of a point where the compressibility is the highest. At $T=2800$ K this point occurs at $P=0.2$ Pa as a consequence of the fact that the free energy surface curvature is very low and therefore the compressibility is large.

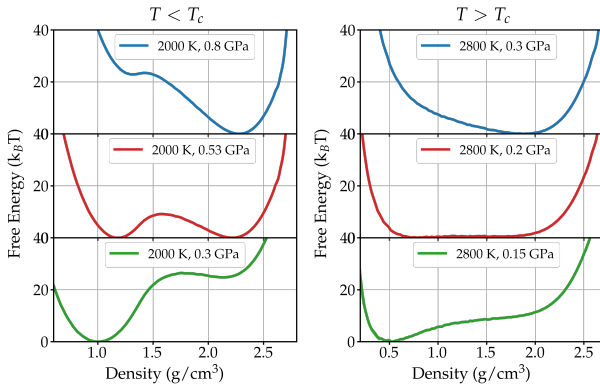


Figure 1: Free-energy surfaces (FESs) as a function of the density for $T = 2000$ K ($T < T_c$) (left) and $T = 2800$ K ($T > T_c$) (right). For each T , three FESs at different P values are shown. Error bars, calculated using the weighted block-average technique (number of blocks = 4) discussed in Ref. 42, are smaller than the linewidth.

This analysis can be repeated at all desired temperatures and pressures in the pressigned MultiTP range and leads to the phase diagram in Fig. 2. In agreement with experiments, the coexistence line has a negative slope. It can be clearly seen that there is a density jump across the phase transition line. As the system approaches the critical point (whose position will be determined below) the jump

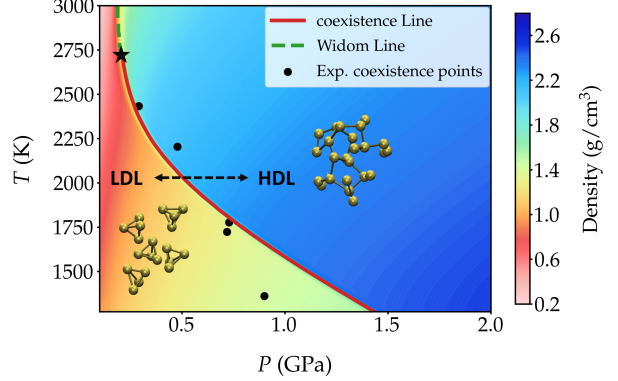


Figure 2: Liquid phosphorus phase diagram: The value of the density as a function of T and P is also plotted. The LL coexistence line is shown in red line. Black points denote the experimental coexistence points. The calculated LL critical point is indicated by the black star, and the Widom line (discussed also in section S4.1 in SI) is shown in dashed green line. Typical structures of the molecular and polymeric phases are depicted in ball-and-stick.

eventually vanishes. In the same picture we also show two typical structural units of LDL and HDL. In LDL, the structural units are P_4 molecules while the HDL phase is characterized by the presence of small irregular branched multimer of different sizes that continuously form and break. One such multimer is shown in the picture. As we approach the critical point from the LDL side we see (see Fig. S9 in SI) that more and more P_4 units are broken. This is to be contrasted with what happens on the HDL side where the multimeric structure is maintained until one gets rather close to the critical point.

We now focus on the transition region. To this effect, we show in Fig. 3 the free energy profiles evolution along the coexistence curve. At the lower temperatures the LDL and HDL minima are well separated reflecting the presence of a first-order transition. However, as the temperature is increased, the barrier between the two phases vanishes and the two phases can no longer be distinguished. The barrier-less transition between the two regimes identifies the critical point. However, reading its precise position from Fig. 3 is difficult and in addition one expects large finite size effects. For this reason we made a Binder cumulant analysis (see section S4.2 in SI)^{50,51} that allows computing the thermodynamic value of the critical point. In such a way we estimate for the critical temperature and pressure the values $T_c \sim 2690$ K and $P_c \sim 0.2$ GPa (see Fig. S7 in SI), that are in line with the indirect one suggested by the experimentalists.¹⁹

It is fascinating to study the evolution of the electronic structure as reflected in the electronic density of states (DOS) and the inverse participation ratio (see section S4.3 in SI). We perform this analysis computing the electronic structure on selected configurations along the coexistence line.

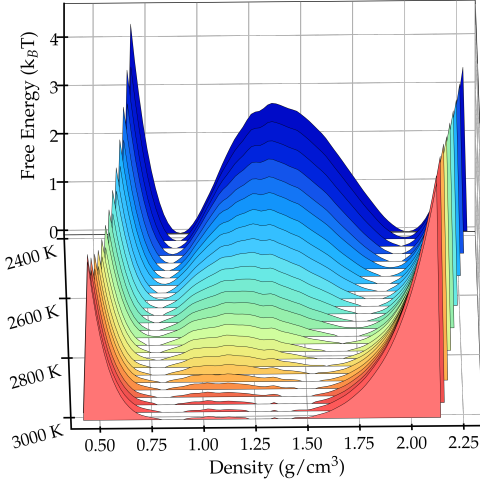


Figure 3: FESs as a function of the density and temperatures along the coexistence line. The color of the FESs varies from blue at $T = 2400$ K to red at $T = 3000$ K.

Deep into the two-phase region, the LDL DOS clearly shows a gap (see Fig. 4 (top)) and the occupied states are well localized as to be expected from a molecular liquid. In contrast, the HDL DOS has a metallic character (see Fig. 4 (bottom)) and the electronic states are rather delocalized (see SI). The behavior of the LDL as it approaches T_c is rather intriguing since localized states appear in the bandgap. These states are localized on the partially broken P_4 molecules (Fig. 5), thus they will not contribute to a metal type conductivity. As we further approach T_c the number of broken P_4 molecules increases and so does the number of states in the bandgap (see Fig. S9 in SI). Right at T_c , the electronic structure undergoes huge fluctuations

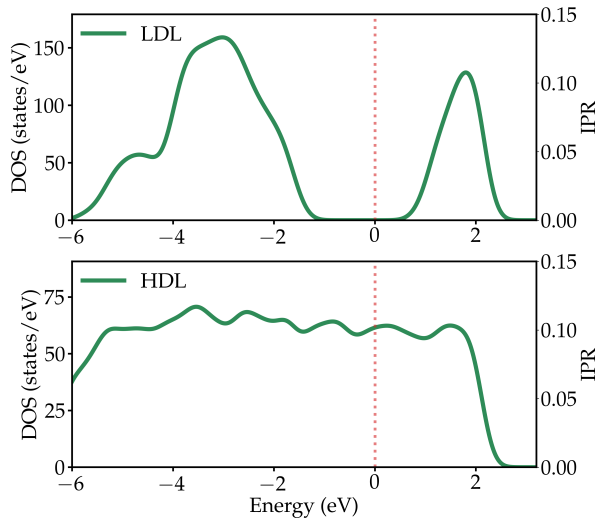


Figure 4: DOS for configurations in the LDL (top) and HDL (bottom) phase at $T = 1273$ K. The Fermi level is shown in red dashed line.

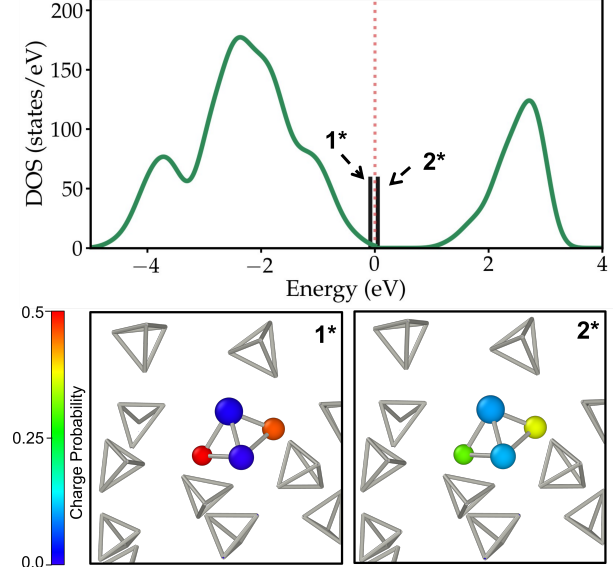


Figure 5: Top: DOS of a defective LDL configuration. The state 1^* and 2^* are localised on a P_4 molecule in which one of the bonds is broken. The Fermi level is shown in red dashed line. The probability density on the unbroken P_4 , represented by stick only, is negligible, while it is significantly large on the broken P_4 , that is represented in (bottom) ball-and-stick.

and goes from a metallic like character to an insulator one (see Fig. S10 in SI), passing *via* intermediate states such as those described above.

Finally, we hope that this fascinating behavior can be experimentally probed since this is an unusual critical system in which a metal non metal transition is strongly coupled to a structural one. The success of our strategy that combines MultiTP-OPES with machine learning encourages us to study in the future even more complex systems.

We thank Michele Invernizzi, Chang Woo Myung, Luigi Bonati, and Omar Abou El Kheir for their help and the many useful discussions. The research was supported by the European Union Grant No. ERC-2014-AdG-670227/VARMET. We also thank the NCCR MARVEL, funded by the Swiss National Science Foundation. The computational resources were obtained from ETH Zurich Euler supercomputer.

References

- [1] Peter H Poole, Francesco Sciortino, Ulrich Essmann, and H Eugene Stanley. Phase behaviour of metastable water. *Nature*, 360(6402):324–328, 1992.
- [2] Francesco Sciortino, Peter H Poole, Ulrich Essmann, and HE Stanley. Line of compressibility maxima in the phase diagram of supercooled water. *Physical Review E*, 55(1):727, 1997.
- [3] Limei Xu and Valeria Molinero. Is there a liquid-liquid transition in confined water? *Journal of Physical Chemistry B*, 115(48):14210–14216, 2011.
- [4] Jeremy C Palmer, Fausto Martelli, Yang Liu, Roberto Car, Athanassios Z Panagiotopoulos, and Pablo G Debenedetti. Metastable liquid–liquid transition in a molecular model of water. *Nature*, 510(7505):385–388, 2014.
- [5] Frank Smallenburg and Francesco Sciortino. Tuning the liquid-liquid transition by modulating the hydrogen-bond angular flexibility in a model for water. *Physical review letters*, 115(1):015701, 2015.
- [6] Peter H. Poole, Richard K. Bowles, Ivan Saika-Voivod, and Francesco Sciortino. Free energy surface of ST2 water near the liquid-liquid phase transition. *Journal of Chemical Physics*, 138(3), 2013.
- [7] Thomas E Gartner, Linfeng Zhang, Pablo M Piaggi, Roberto Car, Athanassios Z Panagiotopoulos, and Pablo G Debenedetti. Signatures of a liquid–liquid transition in an *ab-initio* deep neural network model for water. *Proceedings of the National Academy of Sciences*, 117(42):26040–26046, 2020.
- [8] José L.F. Abascal and Carlos Vega. Widom line and the liquid-liquid critical point for the TIP4P/2005 water model. *Journal of Chemical Physics*, 133(23), 2010.
- [9] Pablo G. Debenedetti, Francesco Sciortino, and Gül H. Zerze. Second critical point in two realistic models of water. *Science*, 369(6501):289–292, 2020.
- [10] Noel Jakse and A Pasturel. Liquid-liquid phase transformation in silicon: evidence from first-principles molecular dynamics simulations. *Physical review letters*, 99(20):205702, 2007.
- [11] Vishwas V Vasisht, Shibu Saw, and Srikanth Sastry. Liquid–liquid critical point in supercooled silicon. *Nature Physics*, 7(7):549–553, 2011.
- [12] Vasily Dzyabura, Mohamed Zaghoo, and Isaac F Silvera. Evidence of a liquid–liquid phase transition in hot dense hydrogen. *Proceedings of the National Academy of Sciences*, 110(20):8040–8044, 2013.
- [13] Erik Lascaris. Tunable liquid-liquid critical point in an ionic model of silica. *Physical review letters*, 116(12):125701, 2016.
- [14] Rei Kurita and Hajime Tanaka. Critical-like phenomena associated with liquid-liquid transition in a molecular liquid. *Science*, 306(5697):845–848, 2004.
- [15] Rei Kurita and Hajime Tanaka. On the abundance and general nature of the liquid–liquid phase transition in molecular systems. *Journal of Physics: Condensed Matter*, 17(27):L293, 2005.
- [16] Matej Huš and Tomaz Urbic. Existence of a liquid-liquid phase transition in methanol. *Physical Review E*, 90(6):062306, 2014.
- [17] Yoshinori Katayama, Takeshi Mizutani, Wataru Utsumi, Osamu Shimomura, Masaaki Yamakata, and Ken Ichi Funakoshi. A first-order liquid-liquid phase transition in phosphorus. *Nature*, 403(6766):170–173, 2000.
- [18] Yoshinori Katayama, Yasuhiro Inamura, Takeshi Mizutani, Masaaki Yamakata, Wataru Utsumi, and Osamu Shimomura. Macroscopic separation of dense fluid phase and liquid phase of phosphorus. *Science*, 306(5697):848–851, 2004.
- [19] G Monaco, S Falconi, WA Crichton, and M Mezouar. Nature of the first-order phase transition in fluid phosphorus at high temperature and pressure. *Physical review letters*, 90(25):255701, 2003.
- [20] Tetsuya Morishita. Liquid-liquid phase transitions of phosphorus via constant-pressure first-principles molecular dynamics simulations. *Physical review letters*, 87(10):105701, 2001.
- [21] Luca M Ghiringhelli and Evert Jan Meijer. Phosphorus: First principle simulation of a liquid–liquid phase transition. *The Journal of chemical physics*, 122(18):184510, 2005.
- [22] Luca M Ghiringhelli and Evert Jan Meijer. Simulating the phosphorus fluid–liquid phase transition up to the critical point. *Journal of Physics: Condensed Matter*, 19(41):416104, 2007.
- [23] G Zhao, H Wang, DM Hu, MC Ding, XG Zhao, and JL Yan. Anomalous phase behavior of first-order fluid-liquid phase transition in phosphorus. *The Journal of chemical physics*, 147(20):204501, 2017.
- [24] Jörg Behler and Michele Parrinello. Generalized neural-network representation of high-dimensional potential-energy surfaces. *Physical Review Letters*, 98(14):1–4, 2007.
- [25] Jörg Behler. Perspective: Machine learning potentials for atomistic simulations. *Journal of Chemical Physics*, 145(17), 2016.
- [26] Jörg Behler. Neural network potential-energy surfaces in chemistry: a tool for large-scale simulations. *Physical Chemistry Chemical Physics*, 13(40):17930–17955, 2011.
- [27] Kun Yao, John E Herr, David W Toth, Ryker Mckintyre, and John Parkhill. The tensormol-0.1 model

- chemistry: a neural network augmented with long-range physics. *Chemical science*, 9(8):2261–2269, 2018.
- [28] Jörg Behler. First principles neural network potentials for reactive simulations of large molecular and condensed systems. *Angewandte Chemie International Edition*, 56(42):12828–12840, 2017.
- [29] Bingqing Cheng, Guglielmo Mazzola, Chris J Pickard, and Michele Ceriotti. Evidence for supercritical behaviour of high-pressure liquid hydrogen. *Nature*, 585(7824):217–220, 2020.
- [30] Justin S Smith, Olexandr Isayev, and Adrian E Roitberg. Ani-1: an extensible neural network potential with dft accuracy at force field computational cost. *Chemical science*, 8(4):3192–3203, 2017.
- [31] Lin Shen, Jingheng Wu, and Weitao Yang. Multi-scale quantum mechanics/molecular mechanics simulations with neural networks. *Journal of chemical theory and computation*, 12(10):4934–4946, 2016.
- [32] Lin Shen and Weitao Yang. Molecular dynamics simulations with quantum mechanics/molecular mechanics and adaptive neural networks. *Journal of chemical theory and computation*, 14(3):1442–1455, 2018.
- [33] Luigi Bonati and Michele Parrinello. Silicon liquid structure and crystal nucleation from *ab initio* deep metadynamics. *Physical review letters*, 121(26):265701, 2018.
- [34] Haiyang Niu, Luigi Bonati, Pablo M Piaggi, and Michele Parrinello. *Ab-initio* phase diagram and nucleation of gallium. *Nature communications*, 11(1):1–9, 2020.
- [35] Manyi Yang, Luigi Bonati, Daniela Polino, and Michele Parrinello. Using metadynamics to build neural network potentials for reactive events: the case of urea decomposition in water. *Catalysis Today*, 2021.
- [36] Linfeng Zhang, Jiequn Han, Han Wang, Roberto Car, and E Weinan. Deep potential molecular dynamics: a scalable model with the accuracy of quantum mechanics. *Physical review letters*, 120(14):143001, 2018.
- [37] Linfeng Zhang, Jiequn Han, Han Wang, Wissam A. Saidi, Roberto Car, and E. Weinan. End-to-end symmetry preserving inter-atomic potential energy model for finite and extended systems. *Advances in Neural Information Processing Systems*, 31:4436–4446, 2018.
- [38] Volker L Deringer, Miguel A Caro, and Gábor Csányi. A general-purpose machine-learning force field for bulk and nanostructured phosphorus. *Nature communications*, 11(1):1–11, 2020.
- [39] Pablo M. Piaggi and Michele Parrinello. Multithermal-multibaric molecular simulations from a variational principle. *Phys. Rev. Lett.*, 122:050601, Feb 2019.
- [40] Pablo M Piaggi and Michele Parrinello. Calculation of phase diagrams in the multithermal-multibaric ensemble. *The Journal of chemical physics*, 150(24):244119, 2019.
- [41] Pablo M Piaggi and Michele Parrinello. Multithermal-multibaric molecular simulations from a variational principle. *Physical review letters*, 122(5):050601, 2019.
- [42] Michele Invernizzi, Pablo M Piaggi, and Michele Parrinello. Unified approach to enhanced sampling. *Physical Review X*, 10(4):041034, 2020.
- [43] Alessandro Laio and Michele Parrinello. Escaping free-energy minima. *Proceedings of the National Academy of Sciences*, 99(20):12562–12566, 2002.
- [44] Alessandro Barducci, Giovanni Bussi, and Michele Parrinello. Well-tempered metadynamics: a smoothly converging and tunable free-energy method. *Physical review letters*, 100(2):020603, 2008.
- [45] Omar Valsson, Pratyush Tiwary, and Michele Parrinello. Enhancing important fluctuations: Rare events and metadynamics from a conceptual viewpoint. *Annual review of physical chemistry*, 67:159–184, 2016.
- [46] Michele Invernizzi and Michele Parrinello. Rethinking metadynamics: from bias potentials to probability distributions. *The journal of physical chemistry letters*, 11(7):2731–2736, 2020.
- [47] Haiyang Niu, Pablo M Piaggi, Michele Invernizzi, and Michele Parrinello. Molecular dynamics simulations of liquid silica crystallization. *Proceedings of the National Academy of Sciences*, 115(21):5348–5352, 2018.
- [48] Linfeng Zhang, De-Ye Lin, Han Wang, Roberto Car, and E Weinan. Active learning of uniformly accurate interatomic potentials for materials simulation. *Physical Review Materials*, 3(2):023804, 2019.
- [49] Yuzhi Zhang, Haidi Wang, Weijie Chen, Jinzhe Zeng, Linfeng Zhang, Han Wang, and E Weinan. DP-GEN: A concurrent learning platform for the generation of reliable deep learning based potential energy models. *Computer Physics Communications*, 253:107206, 2020.
- [50] K. Binder. Critical properties from Monte Carlo coarse graining and renormalization. *Phys. Rev. Lett.*, 47:693–696, Aug 1981.
- [51] Hiroshi Watanabe, Nobuyasu Ito, and Chin-Kun Hu. Phase diagram and universality of the Lennard-Jones gas-liquid system. *The Journal of chemical physics*, 136(20):204102, 2012.

Supporting Information:

Liquid-Liquid Critical Point in Phosphorus

Manyi Yang, Tarak Karmakar, and Michele Parrinello*

Italian Institute of Technology, Via Melen 83, 16152 Genova, Italy

E-mail: michele.parrinello@iit.it

Contents

1	Computational details	S-2
1.1	System setup and equilibration	S-2
1.2	AIMD simulations	S-2
1.3	DFT energy and force calculations	S-3
1.4	MuiltTP-OPES simulations	S-4
1.5	DeepMD setup	S-5
2	NN potential training and validation	S-5
2.1	Collecting training set configurations	S-5
2.2	Training NN models	S-10
2.3	Evaluation of NN models	S-10
3	MultiTP OPES simulations	S-12
4	Additional results	S-13
4.1	Widom line	S-13

4.2	Binder parameters	S-13
4.3	Density of states and inverse participation ratio	S-15
4.4	Temperature-dependented structural evolution	S-17
4.5	Structural evolution in the critical region	S-18

References	S-19
-------------------	-------------

1 Computational details

1.1 System setup and equilibration

The initial structures of the LDL phase was obtained by placing randomly 32 P_4 molecules (128 phosphorus atoms) in a periodically repeated cubic box. In order to remove any non-physical contacts, we optimized this initial structure. Subsequently, we carried out AIMD NVT simulation at $T = 1273$ K followed by a NPT equilibration at $P = 0.85$ GPa. In order to obtain an initial HDL, a LDL configuration was brought to $T = 1500$ K and $P = 5$ GPa. The structure thus obtained was equilibrated following a schedule similar to that applied to the LDL phase.

1.2 AIMD simulations

All AIMD simulations (NVT and NPT) were run using the CP2K software.^{S1} In these runs, the Perdew–Burke–Ernzerh (PBE) exchange-correlation density functional was used.^{S2} The Kohn and Sham orbitals were expanded in a m-DZVP Gaussian basis while the plane wave expansion of the electronic density was truncated at an energy cutoff of 300 Ry. The core electrons were treated using the Goedecker-Teter-Hutter (GTH) pseudopotentials^{S3,S4} optimized for PBE. To deal with the metallic configurations, we adopted a Fermi Dirac smearing of the occupation number of 0.2585 eV around the Fermi energy. To reduce the computational cost, only the Γ -point was used to sample the supercell Brillouin zone.

A time step of 2.0 fs was used in all AIMD simulations. Temperatures and pressures were controlled using Nosé-Hoover thermostat^{S5} and a Nosé-Hoover-like barostat^{S6} with coupling constants of 0.05 ps and 0.5 ps, respectively.

1.3 DFT energy and force calculations

Single point energies and forces were calculated using two exchange-correlation density functionals, PBE^{S2} and Strongly Constrained and Appropriately Normed (SCAN),^{S7} and their two variants obtained by adding a D3 dispersion corrections.^{S8} Specifically, four different DFT methods, PBE, PBE+D3, Scan, Scan+D3, were used. In all cases, the core electrons were described using the GTH pseudopotential^{S3,S4} adapted to the different exchange-correlation functionals used. The smearing parameter is same as that of the AIMD simulations. However, the energy cutoff for PBE and SCAN-based calculations were increased to 400 and 700 Ry, respectively. Additionally, we used k -points grids of $2 \times 2 \times 2$. These setups provide more accurate results (see Fig. S1).

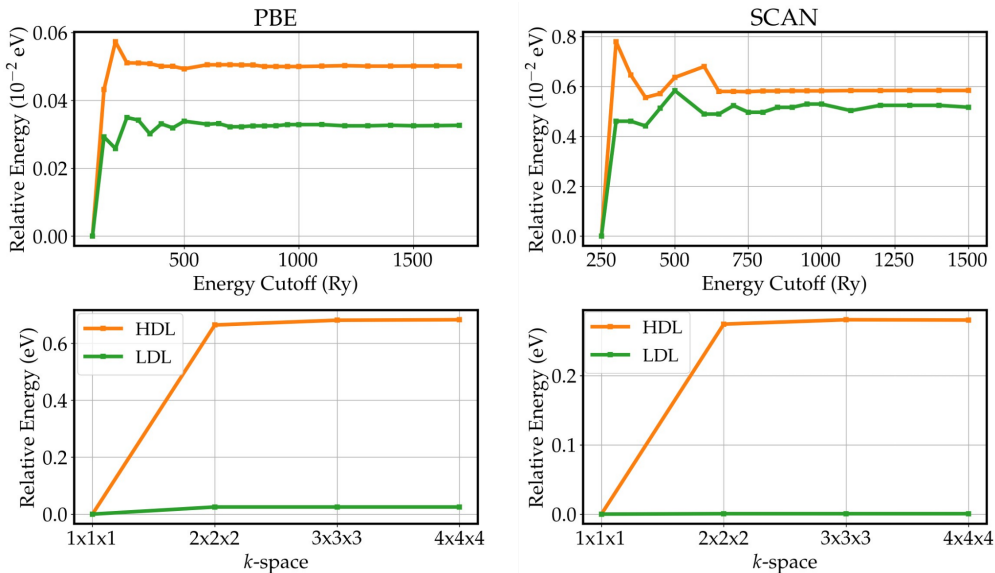


Figure S1: The convergence test for the energy cutoff and the k -space with the PBE and SCAN functionals

1.4 MultTP-OPES simulations

In the MultiTP-OPES simulation one runs an appropriately biased simulation at reference temperature T_0 and pressure P_0 . The bias is crafted such that after reweighing the properties of the system in a whole range of temperatures ($T_{min} < T_0 < T_{max}$) and pressures ($P_{min} < T_0 < P_{max}$) can be recovered. Details of this procedure can be found in Ref. S9 and S10.

In addition, since we want to drive transitions from one phase to the other, we enhanced the fluctuations of the intensity of the first peak ($q = 1.2 \text{ \AA}^{-1}$) of the Debye structure factor (Fig. 1) that has contrasting values in the two liquid phases, and it was used here as a CV. The Debye structure factor is defined as:

$$S(q) = \frac{1}{N} \sum_{i=1}^N \sum_{j=1}^N \frac{\sin(q \cdot r_{ij})}{q \cdot r_{ij}} \quad (1)$$

where, q is the modulus of scattering wave vector, and r_{ij} are the pair-wise distances.

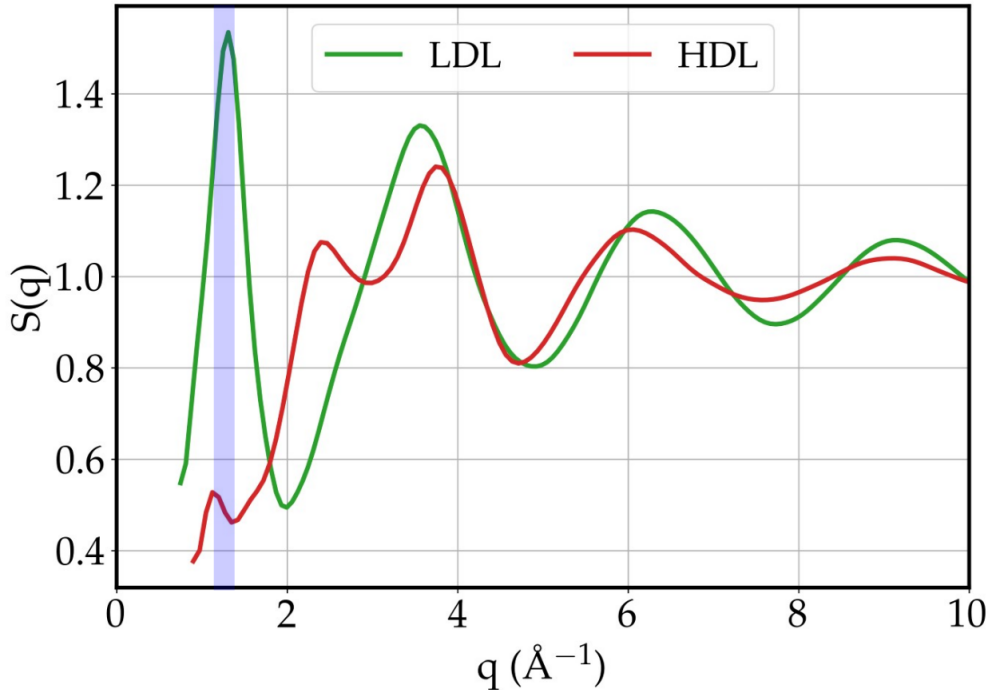


Figure S2: Debye structure factor profiles for the LDL and HDL phases. The transparent blue slab marks the first peak whose intensity was used as a CV for the MultiTP-OPES simulations.

The MultiTP-OPES simulations were run by patching the DeepMD-kit software^{S11} implemented in LAMMPS^{S12} into a development version of PLUMED.^{S13} Temperature and pressure were controlled using the Nosé-Hoover thermostat^{S5} and the Parrinello-Rahman barostat^{S14} with the relaxation times of 0.1 ps and 0.5 ps, respectively. A time step of 1.0 fs was used in all calculations.

In this work, we run MultiTP-OPES simulations in two cases. The first one is used in the DP-GEN iteration steps to sample the atomic configuration space (see section S2.1). The second one is utilized in the production simulations using the final NN models to study the phase diagram of liquid phosphorus (discussed in Section S3).

1.5 DeepMD setup

The NN potentials were trained using the DeepPot-SE (Deep Potential-Smooth Edition) model^{S15} with the DeePMD-kit package.^{S11} The cutoff radius smoothly decays from 5.5 Å to 6.5 Å. We used three hidden layers with (25, 50, 100) nodes/layer for the embedding network and four hidden layers with (240, 240, 240, 240) nodes/layer for the fitting network. The learning rate decays from 1.0×10^{-3} to 5.0×10^{-8} . The batch size was set to 1. The prefactors of the energy and the force terms in the loss function change from 0.1 to 1 and from 1000 to 1, respectively. For the PBE and PBE+D3 NN models, we have included the virial term with prefactor value changing from 0.02 to 0.2 in the loss function,.

2 NN potential training and validation

2.1 Collecting training set configurations

We have used an active learning procedure augmented with MultiTP-OPES method. This strategy, implemented within the DP-GEN package,^{S16} allows us to collect configurations spanning a large area of the phase diagram. The active learning flowchart is shown in Fig. S3. In what follows are the details of the active learning procedure.

First we collected configurations from series of AIMD NPT and NVT simulations (see Section S1.2). The NPT simulations were performed in a range of temperatures from 1273 K to 3000 K and pressures from 0.1 GPa to 2.0 GPa. We also performed NVT simulations at temperatures ranging from 1273 K to 3000 K starting from the HDL phase with varying box lengths from 15.5 to 19.0 Å that corresponds to the density range 1.77 to 0.96 g/cm³; these simulations provided some information on the phase transition region as shown in Fig. S4. In total, 32 NPT and 24 NVT simulations were performed. The simulation time in the different runs ranged from 2 to 10 ps. Finally, we have ~ 22700 atomic configurations in the initial training set (see Fig. S4). Subsequently, their PBE energies and forces were calculated.

These configurations, and the relative DFT energies and forces are the inputs of the DP-GEN iterations (see Fig. S3). Each DP-GEN iteration involves following four steps:

- **Step 1:** Train four NN potentials using the same training set but different initial weights (training steps = 1.2×10^6);
- **Step 2:** Run MultiTP-OPES simulations with the updated NN potentials to explore atomic configuration space;
- **Step 3:** Select new relevant configurations based on a selection criteria (discussed later);
- **Step 4:** Calculate atomic energies and forces for the selected configurations using PBE method. Add these configurations, energies, and forces to the training set;

The DP-GEN iterations are continued until proper exploration of the configuration space of our interest is achieved, and the errors in the NN models are minimized (discussed later).

We found that NN potentials trained only on AIMD (NVT and NPT) configuration were not stable, and the MultiTP OPES simulations run with these NN potentials crashed within a very short simulation time. This is due to the fact that the AIMD configurations were

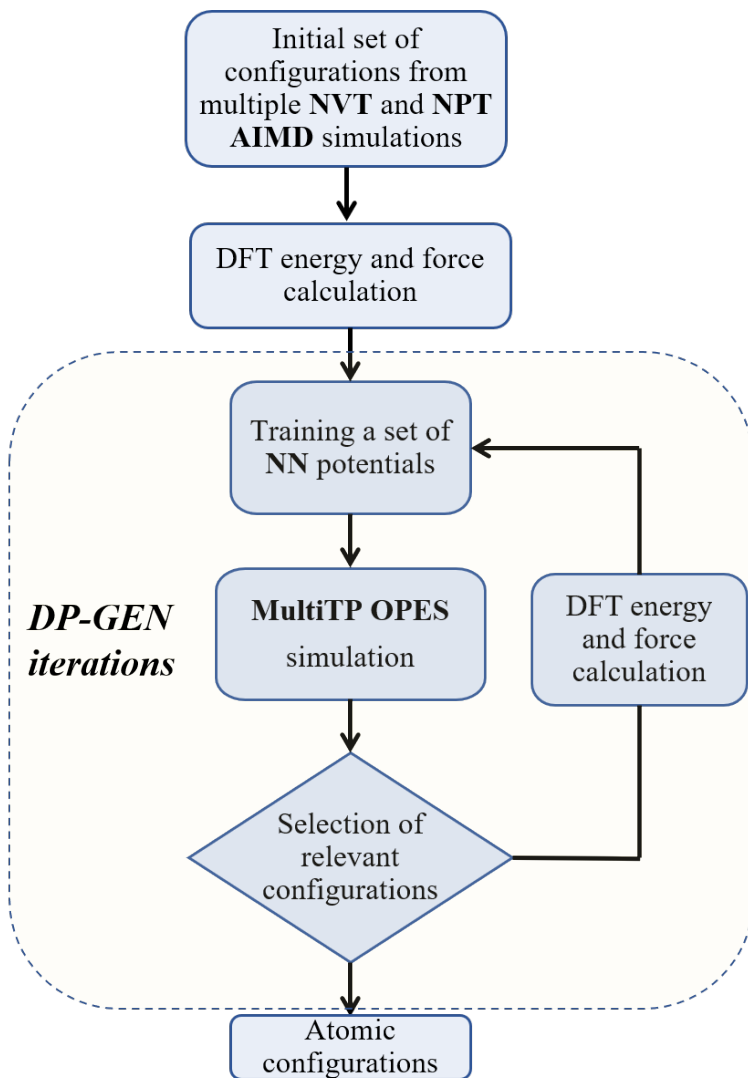


Figure S3: Flowchart for collecting configurations of the training set.

mainly focused on the limited regions of the polymer and P_4 basins and with insufficient configurations in the phase transition region. So for Step 2, in the initial four iterations, we used multiple NPT simulations with NN potentials to enlarge the configuration space. After obtaining slightly more stable NN potentials, we switch to MultiTP-OPES simulations to explore the whole phase diagram configuration space (See Fig. S4). The sampled configurations span a temperature range of 1273 K to 3000 K and pressure range from 0.1 GPa to 5.0 GPa.

The criteria for selecting relevant configurations in Step 3 is based on the model deviation

that is defined by the maximal standard deviation of atomic forces predicted by four different NN potentials that were generated in Step 1. The structures thus generated are labeled according to their model deviations. In our calculations, the structures with model deviations in the range of $[0.2, 0.35]$ eV/Å were labeled as candidate configurations. The lower bound of the model deviation was set to a value that is slightly higher than the average model deviation of the initial training set. The structures with model deviation below the lower bound are already well-represented in the training set. On the other hand, the choice of the upper bound was based on a rule ($[0.15 \sim 0.30 \text{ eV/Å}] + \text{lower bound}$) suggested in Ref. S16. The configurations above the upper bound are non-physical and thus not included in the training set. In each DP-GEN iteration, we run OPES simulations at different thermodynamics conditions. At each thermodynamics condition, we select a maximum of $N_{max} = 250$ and a minimum of $N_{min} = 30$ out of many allowed labeled candidate structures as done in Ref. S17 .

The criteria to stop the DP-GEN iterations is as follows. In each DP-GEN iteration, we monitored the percentage of candidate configurations. Lower the number of newly candidate configurations better is the chance of converged exploration of the configuration space. In our case, once the percentage of candidate configurations reaches $\sim 10\%$ and remains almost unaltered for another few iterations, we exit the loop. This made sure that the configuration space is properly explored. In this way, we collected about 74000 atomic configurations.

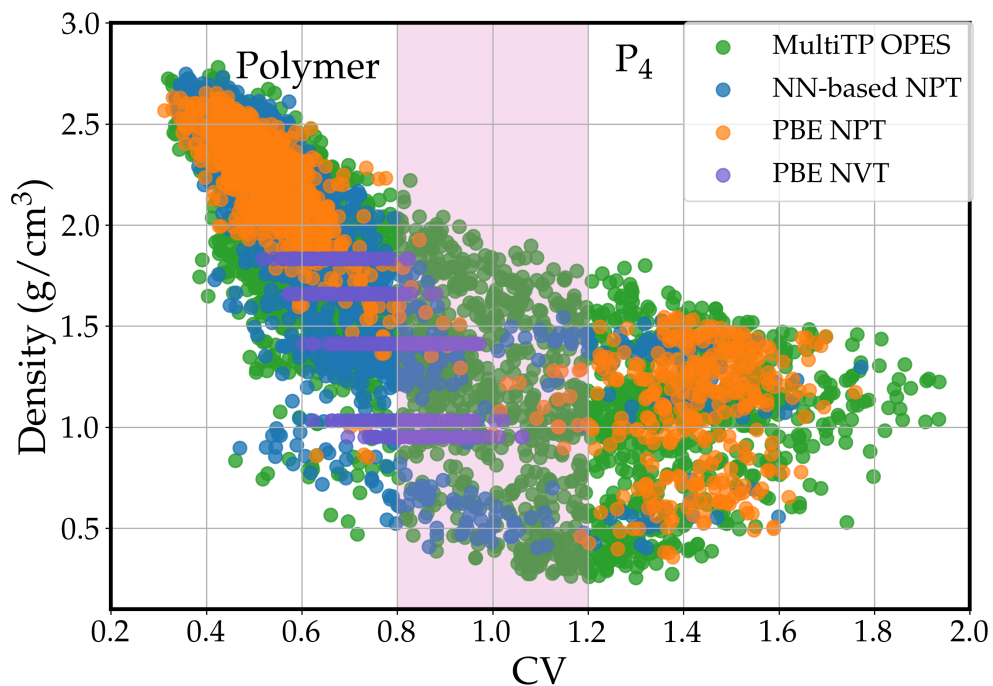


Figure S4: Training set configurations in the CV-Density space: green, blue, orange, and purple points correspond to the configurations sampled *via* MultiTP-OPES, NN-based NPT, PBE NPT, and PBE NVT simulations, respectively. The lower the value of the CV, the more polymer-like a configuration is. The transition state configurations are the ones that have CV range from 0.8 to 1.2 (red shadow marked region).

2.2 Training NN models

With the atomic configurations, energies and forces collected in the previous section, we trained the final PBE-based NN model with long training steps (6.0×10^6). To investigate the effect of different density functionals on the phosphorus NN potential, we obtained three additional NN models that were trained on the same set of configurations but energies and forces calculated using PBE+D3, SCAN, and SCAN+D3 density functionals. Finally, we obtain four NN potentials that are labeled as PBE, PBE+D3, SCAN, and SCAN+D3 models (see Table S1).

2.3 Evaluation of NN models

Mean absolute errors (MAEs) of the final four different NN models prediction in terms of the atomic energies and forces on the test sets are given in Table S1. Configurations in each test set were extracted from the production MultiTP-OPES simulations (discussed in section S3) which were performed using the corresponding NN potentials. For the system containing $N = 128$ phosphorus atoms, each test set sampled ~ 8000 configurations in a range of temperatures $1273 \text{ K} < T < 3000 \text{ K}$ and pressures $0.1 \text{ GPa} < P < 2.0 \text{ GPa}$. For the system of $N = 256$, ~ 800 configurations sampled in a range of temperatures $2400 \text{ K} < T < 3000 \text{ K}$ and pressures $0.1 \text{ GPa} < P < 0.4 \text{ GPa}$ were included.

The comparison of SCAN+D3 DFT and the corresponding NN predicted atomic energies and forces over the test sets is given in Fig. S5. Note that the MAEs of energies in the HDL phase are much higher than that of the LDL phase. We anticipate that the larger MEAs in HDL phase is due the complex coordination environment of the P atoms in the polymeric phase. A similar observation was also reported by Deringer *et al.*^{S18}

Table S1: The MAEs in terms of the atomic energies and forces on the test sets for four different NN models.

Models	MAE of Energy (meV)	MAE of Force (meV/Å)
PBE	23.0	261
PBE+D3	18.4	248
SCAN	20.8	240
SCAN+D3	19.8 (24.4) ^a	227 (283) ^a

^aSystem that contains $N = 256$ phosphorus atoms.

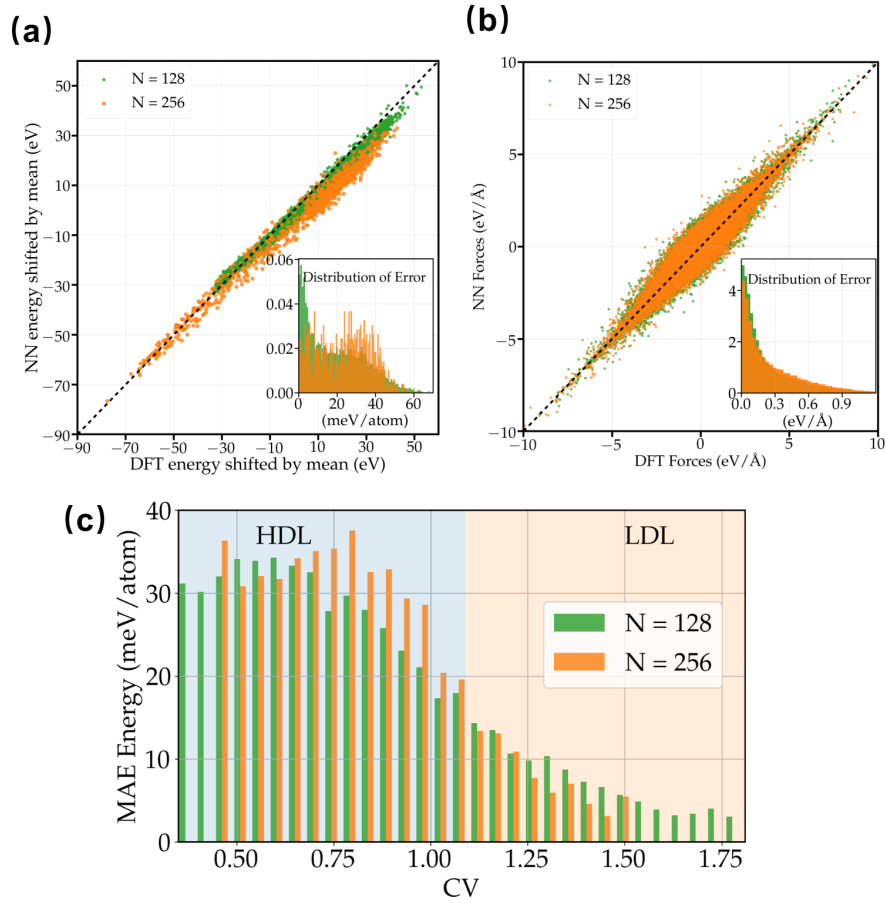


Figure S5: Comparison of atomic energies (a) and forces (b) on test sets calculated by SCAN+D3 DFT method and its corresponding NN model. The configurations in test sets were extracted from the production MultiTP-OPES simulations. Two different systems consisting of $N = 128$ (green) and $N = 256$ (orange) phosphorus atoms were considered. Energies in panel (a) are shifted by the mean value of the DFT energies. Insets in panel (a) and (b) illustrate the probability distributions of the absolute difference in energy and force between the DFT and NN model; (c) The distribution of the MAEs of the energies as a function of the structure factor CV .

3 MultiTP OPES simulations

To explore the whole liquid-liquid phase diagram, we run MultiTP OPES simulations with 128 phosphorus atoms at $T_{min} = 1273 < T_0 = 2200 < T_{max} = 3000$ K and $P_{min} = 0.1 < P_0 = 0.3 < P_{max} = 2.0$ GPa. Four independent MultiTP OPES simulations with the four NN models (PBE, PBE+D3, SCAN, and SCAN+D3) were carried out. After reweighing these simulations, we obtained the liquid-liquid coexistence lines that are shown in Fig. S6. It is clear that the PBE and SCAN+D3 based NN models best approximate the experimental coexistence points.

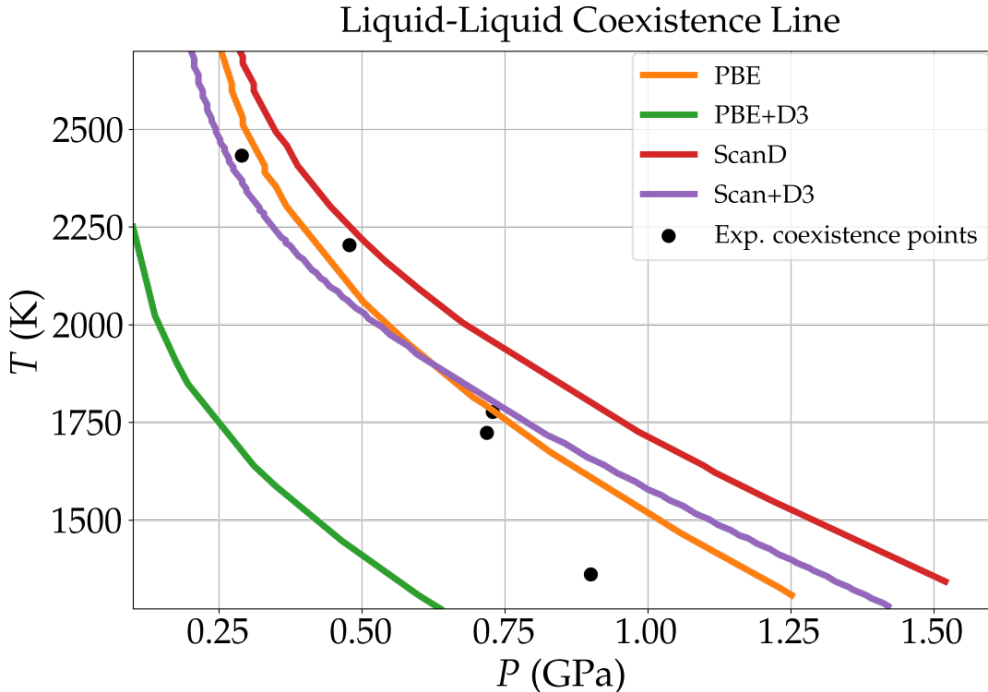


Figure S6: Comparison of the liquid-liquid coexistence line of phosphorus calculated by MultiTP-OPES with different NN models (PBE, PBE+D3, SCAN, and SCAN+D3). Black points denote the experimental coexistence points.

We carried out additional MultiTP OPES simulations with the SCAN+D3 NN model mainly focusing on the critical region to locate the critical point. In these simulations, we considered a temperature range 2400 to 3000 K and pressure range 0.1 to 0.4 GPa with the reference temperature $T_0 = 2600$ K and pressure $P_0 = 0.15$ GPa. The calculated free energy

surfaces are presented in Fig. 3 of the main text.

As we have mentioned in the main text, the free energy barrier height between the LDL and HDL phases depends on the system size. For this reason, we performed additional simulations with larger systems containing 256 and 512 phosphorus atoms focusing on the critical region. These simulations were utilized to calculate the system-size dependent Binder parameter as discussed in Section S4.2.

In both sets of MultiTP-OPES simulations, we have used four walkers that share the same bias. The simulations length ranges from 75 to 100 ns.

4 Additional results

4.1 Widom line

We calculated the Widom line as the locus of the compressibility maxima K_T^{max} for $T \geq T_c$. To locate the Widom line, first we calculated the compressibility K_T from the fluctuations of volume V (NPT simulations) using the equation:

$$K_T = \frac{\langle V^2 \rangle - \langle V \rangle^2}{\langle V \rangle k_B T} \quad (2)$$

where $\langle V \rangle$ is the ensemble average of V and k_B is the Boltzmann constant.

For every T and P points in the predefined TP range, the corresponding K_T can be obtained by reweighing the MultiTP-OPES simulations. At each T , we plotted the K_T as a function of P . Projecting the maximum K_T of these profiles (K_T^{max}) on the TP plane provides the Widom line as shown in Fig. 2 of the main text.

4.2 Binder parameters

We located the critical point using the Binder parameter (U_N). In the scaling limit, U_N for systems of different number of particles N is expected to intersect at a common point, that

corresponds to the critical point. The U_N is calculated using the following equation,

$$U_N = 1 - \frac{\langle \rho^4 \rangle_N}{3 \langle \rho^2 \rangle_N^2} \quad (3)$$

where, $\langle \rho^k \rangle_N = \int (\rho - \bar{\rho})^k \mathbf{P}_N(\rho) d\rho$, $k = 2, 4$ is the k -th moment of the density, ρ . The $\bar{\rho}$ and $\mathbf{P}_N(\rho)$ in the integrand are the expectation value and the distribution function of ρ .

We obtained the values of $U_N(T, P)$ as a function of T and P on the phase diagram by reweighing the MultiTP OPES simulations. Then, we extracted the values of $U_N(T, P)$ along those T and P in which the compressibility is maximum K_T^{max} .

Following this strategy, we calculated the U_N for the three systems with $N = 128, 256$, and 512 phosphorus atoms. From Fig. S7 we can see that these three curves approximately intersect at one point that corresponds to the critical point $T_c \sim 2690$ K and $P_c \sim 0.2$ GPa.

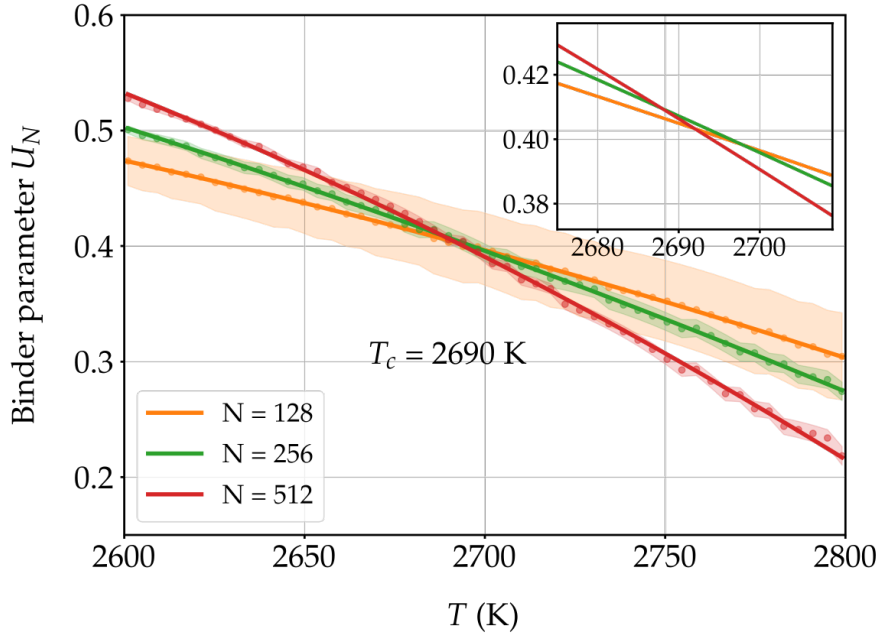


Figure S7: Binder parameter U_N as a function of the temperature T , for different system sizes $N = 128, 256$, and 512. The solid lines are the second degree polynomial fitting of the raw data. The shaded areas indicate the statistical error calculated using the weighted block-average technique (number of blocks = 4) discussed in Ref. S10.

4.3 Density of states and inverse participation ratio

We studied the electronic property of liquid phosphorus by calculating the electronic density of states (DOS) for configurations in HDL and LDL phases as well as those along the coexistence line. Furthermore, to quantify the localisation of the electronic states, we calculated the inverse participation ratio (IPR). The IPR for the n th eigenstate ψ_n is given as,

$$IPR(\psi_n) = \frac{\sum_{i=1}^N |\phi_{n,i}|^4}{(\sum_{i=1}^N |\phi_{n,i}|^2)^2} = \sum_{i=1}^N |q_{n,i}|^2 \quad (4)$$

where $\phi_{n,i}$ is the projected coefficient of the i th basis set orbital in the n th Kohn–Sham eigenstate ψ_n . The $q_{n,i}$ is the probability of finding the (normalized) eigenstate ψ_n in basis set orbital i . If the eigenstate is ideally localised at one particular basis orbital i , the corresponding IPR is equal to one. On the contrary, the IPR for the equally delocalised state is equal to $1/N$, namely, a higher IPR signifies a higher degrees of localization.

To calculate the DOS and IPR, we first run a self-consistent calculation using a k -points grid of $2 \times 2 \times 2$ to generate electron density, and then performed another non-self-consistent calculation with a k -points grid of $4 \times 4 \times 4$. All simulations were performed with the Quantum Espresso 6.6 package.^{S19–S21} We used a cubic system consisting of 128 phosphorus atoms, PBE exchange-correlation functional, and the PAW pseudopotential. we set the plane-wave cutoff as 40 Rydberg (Ry) and the DOS were calculated using Gaussian smearing with broadening at 0.3 eV.

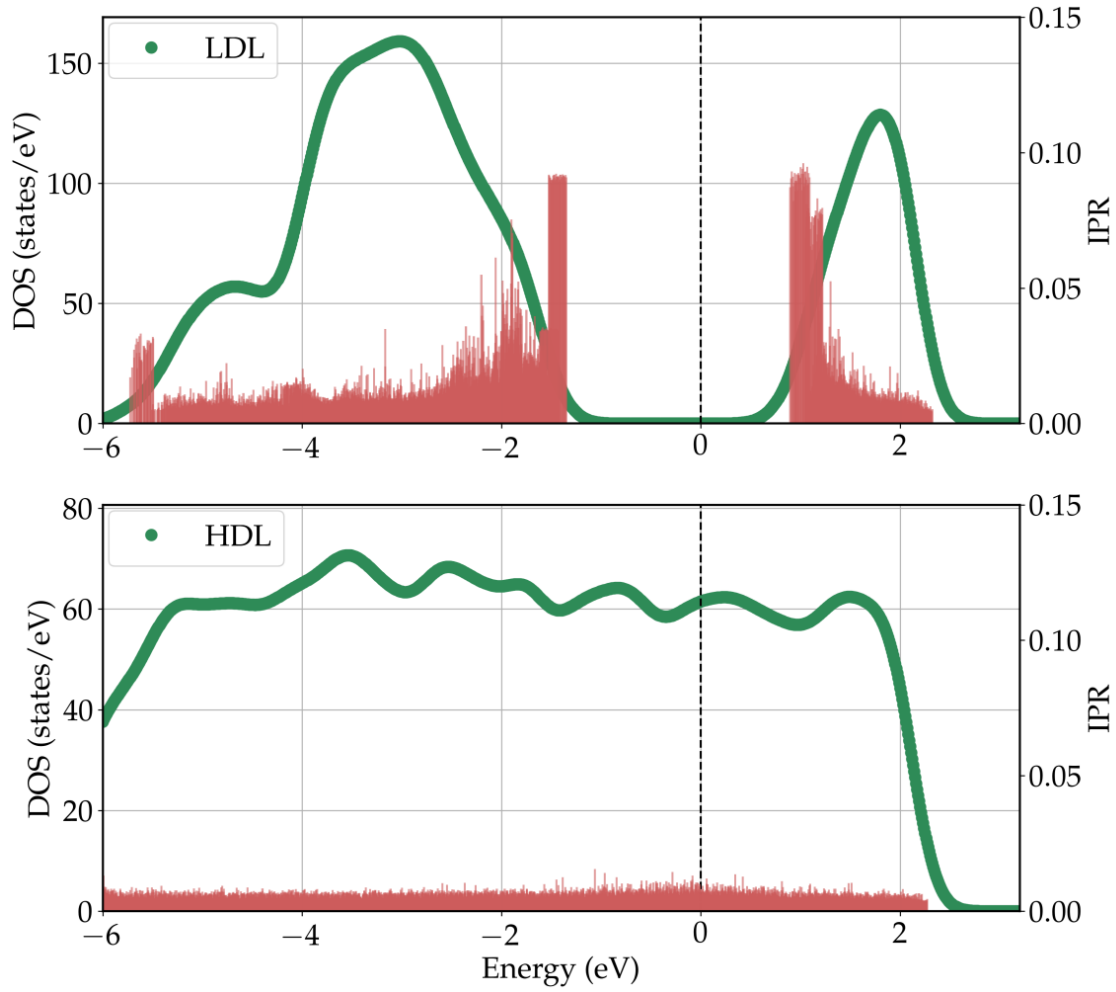


Figure S8: The total DOS (Green line) and IPR (Red spikes) for configurations in the LDL (top) and HDL (bottom) phase at $T = 1273$ K. The Fermi level is shown in black dashed line.

4.4 Temperature-dependented structural evolution

To quantify the structural evolution of the LDL and HDL phase as they approach the critical region, we performed a few standard NPT simulations at different T and P . The number of P_4 molecules is used as a marker. Ideally, the LDL phase should contain 32 P_4 molecular units. As we increase the T from 2000 K to 2600 K the P_4 molecules break resulting in a dramatic reduction of the P_4 count (Fig. S9). On the other hand, the HDL phase retains its polymeric structure until it reaches to 2600 K where a few P_4 molecules appear.

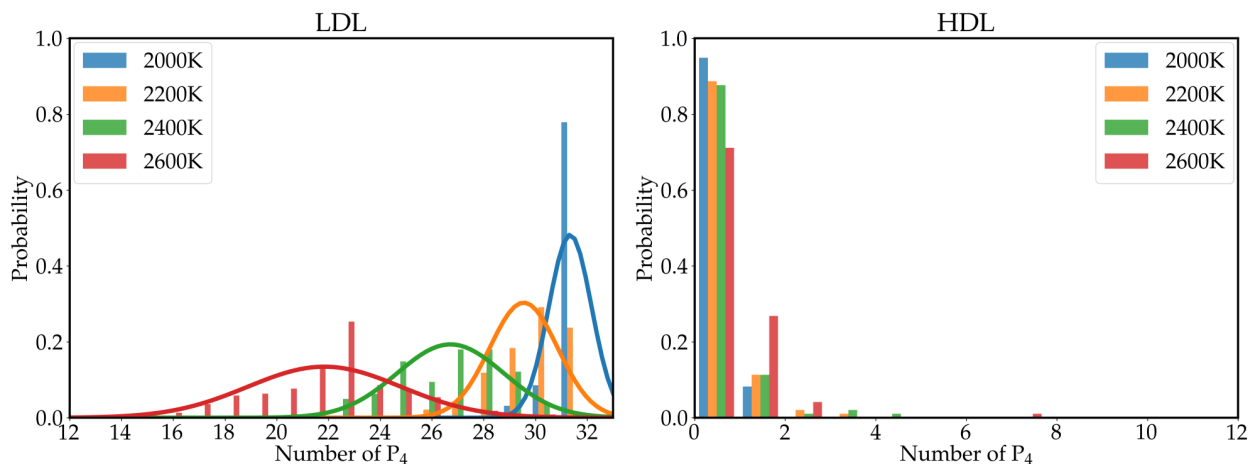


Figure S9: The histogram of the number of P_4 units in each structure as a function of T when we approach the critical point from both the LDL (left) and HDL (right) side. For each thermodynamic condition, 100 structures extracted from 2 ns standard NPT trajectory were analyzed. (For the LDL phase, we increase the T from 2000 K to 2600 K at $P = 0.15$ GPa. Instead, for the HDL phase, the simulations were carried out at various P : 0.53 GPa, 0.45 GPa, 0.35 GPa, and 0.30 GPa.)

4.5 Structural evolution in the critical region

Furthermore, we investigated the structural evolution of the system in the critical region. For this purpose, we run an additional unbiased NPT simulation at $T = 2700$ K and $P = 0.2$ GPa. Fig. S10(a) shows large density fluctuations which is expected for a system in its critical state. Fig. S10(b) shows a typical density evolution as the system transits from the polymeric to molecular phase. The density change accompanies with the transformation

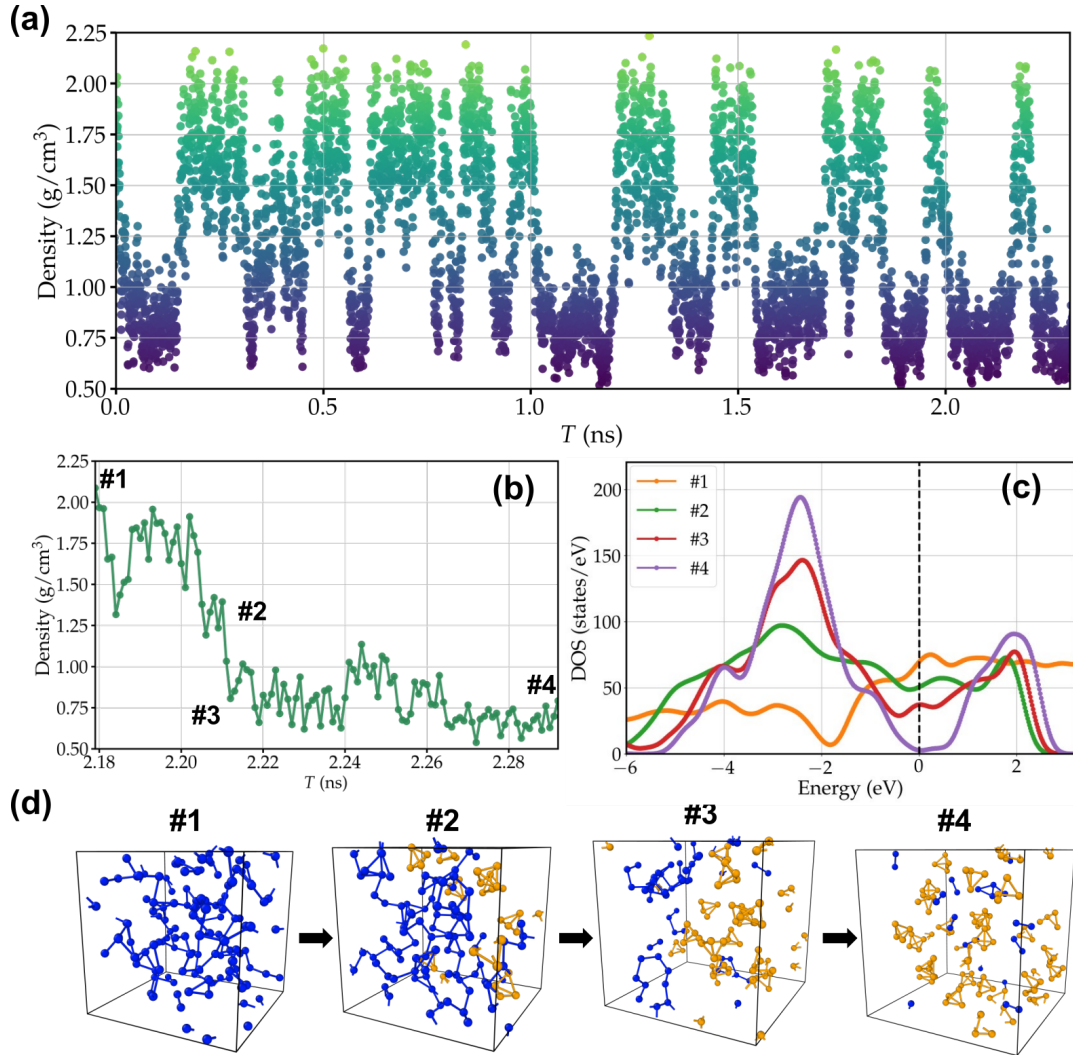


Figure S10: (a) Density as a function of the simulation time obtained from an unbiased NPT simulation run at the $T = 2700$ K and $P = 0.2$ GPa; The evolution of (b) density, (c) DOS, and (d) structures as the system transits from the polymeric to the molecular phase. Atoms belong to polymers are shown in blue while those belong to the P_4 units are displayed in orange.

from the metallic to the non-metallic phase as revealed by the DOS (Fig. S10(c)). The structural evolution going from the polymeric phase (#1) to the molecular phase (#4) via the intermediates (#2 and #3) is illustrated in Fig. S10(d).

References

- (S1) Maintz, S.; Deringer, V. L.; Tchougréeff, A. L.; Dronskowski, R. LOBSTER: A tool to extract chemical bonding from plane-wave based DFT. 2016.
- (S2) Perdew, J. P.; Burke, K.; Ernzerhof, M. *Physical review letters* **1996**, *77*, 3865.
- (S3) Goedecker, S.; Teter, M.; Hutter, J. *Physical Review B* **1996**, *54*, 1703.
- (S4) Hartwigsen, C.; Goedecker, S.; Hutter, J. *Physical Review B* **1998**, *58*, 3641.
- (S5) Evans, D. J.; Holian, B. L. *The Journal of chemical physics* **1985**, *83*, 4069–4074.
- (S6) Melchionna, S.; Ciccotti, G.; Lee Holian, B. *Molecular Physics* **1993**, *78*, 533–544.
- (S7) Sun, J.; Ruzsinszky, A.; Perdew, J. P. *Physical review letters* **2015**, *115*, 036402.
- (S8) Grimme, S.; Ehrlich, S.; Goerigk, L. *Journal of computational chemistry* **2011**, *32*, 1456–1465.
- (S9) Invernizzi, M.; Parrinello, M. *The journal of physical chemistry letters* **2020**, *11*, 2731–2736.
- (S10) Invernizzi, M.; Piaggi, P. M.; Parrinello, M. *Physical Review X* **2020**, *10*, 041034.
- (S11) Wang, H.; Zhang, L.; Han, J.; Weinan, E. *Computer Physics Communications* **2018**, *228*, 178–184.
- (S12) Plimpton, S. *Journal of computational physics* **1995**, *117*, 1–19.

- (S13) Tribello, G. A.; Bonomi, M.; Branduardi, D.; Camilloni, C.; Bussi, G. *Computer Physics Communications* **2014**, *185*, 604–613.
- (S14) Parrinello, M.; Rahman, A. *Journal of Applied physics* **1981**, *52*, 7182–7190.
- (S15) Zhang, L.; Han, J.; Wang, H.; Saidi, W. A.; Car, R.; Weinan, E. *Advances in Neural Information Processing Systems* **2018**, *31*, 4436–4446.
- (S16) Zhang, Y.; Wang, H.; Chen, W.; Zeng, J.; Zhang, L.; Wang, H.; Weinan, E. *Computer Physics Communications* **2020**, *253*, 107206.
- (S17) Yang, M.; Bonati, L.; Polino, D.; Parrinello, M. *Catalysis Today* **2021**,
- (S18) Deringer, V. L.; Bernstein, N.; Csányi, G.; Mahmoud, C. B.; Ceriotti, M.; Wilson, M.; Drabold, D. A.; Elliott, S. R. *Nature* **2021**, *589*.
- (S19) Giannozzi, P.; Baroni, S.; Bonini, N.; Calandra, M.; Car, R.; Cavazzoni, C.; Ceresoli, D.; Chiarotti, G. L.; Cococcioni, M.; Dabo, I.; Dal Corso, A.; de Gironcoli, S.; Fabris, S.; Fratesi, G.; Gebauer, R.; Gerstmann, U.; Gougoussis, C.; Kokalj, A.; Lazzeri, M.; Martin-Samos, L.; Marzari, N.; Mauri, F.; Mazzarello, R.; Paolini, S.; Pasquarello, A.; Paulatto, L.; Sbraccia, C.; Scandolo, S.; Sclauzero, G.; Seitsonen, A. P.; Smogunov, A.; Umari, P.; Wentzcovitch, R. M. *Journal of Physics: Condensed Matter* **2009**, *21*, 395502 (19pp).
- (S20) Giannozzi, P.; Andreussi, O.; Brumme, T.; Bunau, O.; Nardelli, M. B.; Calandra, M.; Car, R.; Cavazzoni, C.; Ceresoli, D.; Cococcioni, M.; Colonna, N.; Carnimeo, I.; Corso, A. D.; de Gironcoli, S.; Delugas, P.; Jr, R. A. D.; Ferretti, A.; Floris, A.; Fratesi, G.; Fugallo, G.; Gebauer, R.; Gerstmann, U.; Giustino, F.; Gorni, T.; Jia, J.; Kawamura, M.; Ko, H.-Y.; Kokalj, A.; Küçükbenli, E.; Lazzeri, M.; Marsili, M.; Marzari, N.; Mauri, F.; Nguyen, N. L.; Nguyen, H.-V.; de-la Roza, A. O.; Paulatto, L.; Poncé, S.; Rocca, D.; Sabatini, R.; Santra, B.; Schlipf, M.; Seitsonen, A. P.; Smo-

gunov, A.; Timrov, I.; Thonhauser, T.; Umari, P.; Vast, N.; Wu, X.; Baroni, S. *Journal of Physics: Condensed Matter* **2017**, *29*, 465901.

(S21) Giannozzi, P.; Baseggio, O.; Bonfà, P.; Brunato, D.; Car, R.; Carnimeo, I.; Cavazzoni, C.; de Gironcoli, S.; Delugas, P.; Ferrari Ruffino, F.; Ferretti, A.; Marzari, N.; Timrov, I.; Urru, A.; Baroni, S. *The Journal of Chemical Physics* **2020**, *152*, 154105.